Journal of Hazardous Materials Advances 22 (2026) 101159

Contents lists available at ScienceDirect

Journal of Hazardous Materials Advances

journal homepage: www.elsevier.com/locate/hazadv

Effect of temperature and P^{5+} ions concentration on the phosphorus adsorption mechanism by synthetic calcium silicate hydrates

Evelina Svedaite [a,*], Kestutis Baltakys [a], Donatas Levisauskas [b], Vytautas Galvanauskas [b], Tadas Dambrauskas [a]

[a] Department of Silicate Technology, Kaunas University of Technology, Radvilenu rd.19, Kaunas, LT-50254, Lithuania
[b] Department of Automation, Kaunas University of Technology, Studentu 48, Kaunas, LT-51367, Lithuania

ARTICLE INFO

Keywords:
Calcium silicate hydrate
Phosphorus
Hydrothermal synthesis
Adsorption
Kinetics

ABSTRACT

Efficient treatment of phosphorus-rich wastewater is crucial for protecting the ecosystem. Several methods have been developed for removing phosphates from aqueous solutions, with adsorption technology among the most effective. The main objective of this work was to synthesize an adsorbent based on calcium silicate hydrates and apply it for the adsorption of phosphate ions. The adsorbent was synthesized from a mixture of CaO and natural opoka under hydrothermal synthesis conditions (16 h, 200 °C). Batch adsorption experiments were carried out at 25, 35, and 45 °C in a thermostatic absorber by stirring 10 g of synthesized adsorbent in 1 L of KH_2PO_4 solution containing 0.2–5 g P^{5+}/L. The adsorption lasted up to 168 h. It was determined that during adsorption, calcium and phosphorus ions interact strongly, leading to the formation of hydroxyapatite and brushite. The adsorbent can adsorb up to 210 mg P^{5+}/g, depending on the adsorption conditions, including adsorption temperature and initial phosphorus content. Adsorption mechanisms were characterized using an adsorption kinetic model and isotherms. The optimal phosphorus uptake rate was calculated using the response surface model.

1. Introduction

Phosphorus (P) is a macronutrient essential for plant growth and is applied as natural and mineral fertilizers to increase crop production (Bus, 2017). Simultaneously, phosphorus is a major environmental contaminant when present in high amounts in aquatic ecosystems (Rezania et al., 2021). The accumulation of phosphorus in aquatic ecosystems is primarily attributable to anthropogenic activities, including agricultural runoff and untreated wastewater discharges. These activities contribute to phosphorus accumulation, leading to eutrophication (Goldsberry et al., 2023; Trotta et al., 2023). Managing phosphorus from both perspectives – reducing its environmental impact and recovering it as a valuable resource – is therefore critical to achieving sustainable development goals (Akinnawo, 2023; Hernández-Alcayaga et al., 2025; Riza et al., 2023).

The removal of phosphorus from wastewater is an ongoing scientific issue with important implications for environmental sustainability and resource use (García-Ávila et al., 2025; Zheng et al., 2023). Several technologies have been developed for phosphorus removal, including physical, chemical, and biological methods (Augustyniak-Tunowska et al., 2023; Singh et al., 2023). Adsorption stands out as a viable solution due to its high efficiency, simplicity of operation, and cost-effectiveness (Hao et al., 2021). Adsorption is mainly controlled by temperature and initial solution concentrations (Gao et al., 2025; Kari-Ferro et al., 2024). Temperature determines the kinetic and thermodynamic behavior of adsorption, influencing adsorption rates, equilibrium, and the stability of adsorbent-adsorbate interactions (Baruah et al., 2025; Nakić et al., 2025). Adsorption is generally accelerated at higher temperatures due to increased molecular mobility and stronger interactions between the adsorbent and the adsorbate (Kong et al., 2025; Soo et al., 2024; Wen et al., 2024). However, high temperatures may compromise the stability of adsorbents or alter their surface properties, potentially reducing adsorption effectiveness (Ozcan et al., 2024). Meanwhile, the concentration of P^{5+} ions influences the availability of adsorbate molecules and the saturation of the adsorbent's active centers (Lade, 2021; Manna et al., 2022). Adsorption at lower P^{5+} concentrations often follows a linear isotherm due to the abundance of active sites (Amarh et al., 2021; Karageorgiou et al., 2007). However, as the concentration increases, these sites may become saturated, reducing adsorption efficacy. The interaction between temperature and initial

---

* Corresponding author.
E-mail address: evelina.svedaite@ktu.lt (E. Svedaite).

https://doi.org/10.1016/j.hazadv.2026.101159
Received 26 August 2025; Received in revised form 6 March 2026; Accepted 7 April 2026

concentration further complicates the process, as high temperatures may reduce the benefits of saturation by increasing desorption rates or altering the adsorbent's surface chemistry (Amarh et al., 2021; Maimulyanti et al., 2022). These properties have been the focus of individual studies in specific circumstances. However, there is still limited understanding of their combined influence on the phosphorus adsorption process (Nguyen et al., 2023; Pimentel Frisancho et al., 2025).

As previously discussed, the adsorption process can be burdened by the saturation of the adsorbent's accessible active sites at high phosphorus concentrations, such as those found in agricultural runoff or wastewater (>10 mg/L). In such contexts, adsorbents based on calcium silicate hydrate are more effective than conventional materials such as clay or synthetic polymers (Samantray et al., 2022; Han et al., 2023). Scientists are increasingly investigating calcium silicates or calcium silicate hydrates (CSH) based adsorbents due to their industrial relevance (Corrado and Polini, 2019; Cui et al., 2024). These materials exhibit high potential for phosphorus removal; for instance, synthetic porous CSH can achieve an adsorption capacity of up to 100 mg/g, exceeding traditional adsorbent capacity values such as natural clays (0.491 mg/g) (Moharami et al., 2013), zeolites (0.37 mg/g) (Salkunić et al., 2022), and fly ash (71.87 mg/g) (Salkunić et al., 2022). During phosphorus adsorption, CSH can recrystallize into hydroxyapatite, reducing phosphorus concentrations from 20 mg/L to below 1 mg/L (Kim et al., 2006; Zheng et al., 2024). Other studies also demonstrate that CSH modification enhances adsorption capacity and efficiency; for example, CSH and cryogel-based or konjac–PVA/CSH composites showed capacities of 12.3–45 mg/g with efficiencies above 94% (Phawachalotorn et al., 2023; Taweekarn et al., 2023; Wu et al., 2024). Metal-modified CSH, such as La–CSH and Zr–CSH, showed even higher capacities, ranging from 282 to 729 mg/g (Huo et al., 2021; Ou et al., 2007; Wujcicki et al., 2023). Despite these promising properties, most research relies on CSH synthesis from pure chemicals or soluble salts using precipitation or sol-gel methods, which limit large-scale applicability (Piao et al., 2020; Wang et al., 2019). Although some studies have synthesized CSH-based adsorbents from natural rocks, these materials generally exhibit limited adsorption investigation across both low and high phosphorus concentrations, and are characterized by incomplete or insufficiently detailed kinetic evaluations (Gizaw et al., 2022; Taweekarn et al., 2022; Zhang et al., 2019). These parameters, however, are essential for engineering effective adsorption systems and ensuring the effective removal of phosphorus under diverse environmental conditions (Mechnou et al., 2025).

Thus, this study aims to determine the influence of temperature, duration, and P^{5+} concentration on the phosphorus adsorption process using calcium silicate mineral-based adsorbents. Furthermore, adsorption isotherms, kinetics, and thermodynamic parameters were estimated from the experimental results.

2. Materials and methods

2.1. Raw materials

In this study, the reagents listed below were used as starting materials for the synthesis of the adsorbent.

- Opoka was crushed (Ecofiltration Sp. z o.o., Poland) using a "Pulverisette 1″ crusher (Fritsch, Germany). The material was then ground for 5 h in a ball mill and subsequently for 5 min at 900 rpm in a vibrating disc mill, "Pulverisette 9" (Fritsch, Germany). The ground opoka was calcined at 850 °C.
- CaO was produced by grinding $CaCO_3$ (Sigma-Aldrich, Japan) at 700 rpm for 1 min in a vibrating disc mill 'Pulverisette 9′ and then calcining the material for 1 h at 950 °C. After calcination, the product contains 95.47 wt% free CaO.
- To prepare an adsorption solution with P^{5+} ions (concentration ranging from 0.2 to 5.0 g P^{5+}/L), KH_2PO_4 (Chempur, Poland, purity 99.5 wt%) was dissolved in distilled water.

2.2. Analytical methods

The phosphorus concentration was measured using the *photocolorimetric method.* This technique relies on the reaction of the phosphate ion with ammonium vanadate and molybdate, producing a yellow phosphorus-molybdenum-vanadium complex (P_2O_5–V_2O_5–$22MoO_3$–H_2O). The color's intensity reflects the P_2O_5 level. The solution's optical density was measured with a UV–VIS T70/T70+ photocolorimeter (PG Instruments Limited, Lutterworth, UK) at 450 nm wavelength.

Simultaneous thermal analysis (STA) was used to analyze the thermal stability of products. Analysis was performed using Linseis PT1000 instrument (Linseis, Germany). The operating conditions: a heating rate of 15 °C/min, a temperature range of 30–1000 °C, a nitrogen atmosphere, ceramic sample holders, Pt crucibles, and a sample mass of ~13 mg.

X-ray powder analysis (XRD) was conducted to identify the mineralogical composition of samples using the D8 Advance diffractometer (Bruker AXS, Karlsruhe, Germany), which operates at a tube voltage of 40 kV and a tube current of 40 mA. The X-ray beam was filtered with a 0.02-mm Ni filter to select the Cu Kα wavelength. Diffraction patterns were recorded in a Bragg–Brentano geometry with a fast-counting detector from Bruker. The LynxEye detector is based on silicon strip technology. The specimens were scanned over a 2θ range of 3–70° at a speed of 6° per minute in coupled two-theta/theta scan mode.

The pH values of samples from adsorption solutions were measured with a Hanna pH meter (Hi 9321, Hanna Instruments, Woonsocket, RI, USA).

The specific surface area of the samples was determined using the Brunauer, Emmett, and Teller (BET) method. Measurements were performed using a Quantachrome AUTOSORB–iQ–K/MP (Quantachrome, USA) device with nitrogen adsorption isotherms at 77 K. Before measurement, samples were degassed at 100 °C. The specific surface area of the samples was calculated with the BET equation by using the data of the lower part of the N_2 adsorption isotherm ($0.05 < p/p_0 < 0.35$) (Thommes et al., 2015):

$$\frac{1}{X\left(\frac{p_0}{p}-1\right)}=\frac{C-1}{X_m\cdot C}\cdot\frac{P}{P_0}+\frac{1}{X_m\cdot C} \tag{1}$$

where X is the mass of the adsorbate adsorbed on the sample at relative pressure p/p_0, p is the partial pressure of the adsorbate, p_0 is the saturated vapour pressure of the adsorbate, X_m is the mass of the adsorbate adsorbed at a coverage of one monolayer, C is a constant which is the function of the heat of adsorbate condensation and the heat of adsorption (C_{BET} is a constant).

FEI Helios Nanolab 650 (FEI, Netherlands, 2011) *scanning electron microscope (SEM)* was used for surface investigation of the samples. The samples were vacuum chromium-coated (Q150T ES, Quorum Technologies Ltd.) and examined in the secondary electron imaging (SEI) mode at an acceleration voltage of 2 kV and a beam current of 25 pA.

Transmission electron microscope (TEM) images were taken using a Tecnai G2 F20 X-TWIN (FEI, Netherlands, 2011) with a Schottky-type field-emission electron source. The accelerating voltage was 200 kV. In order to take TEM images, a high-angle annular dark field detector (HAADFD) was used.

2.3. Synthesis of an adsorbent

The calcium silicate hydrate-based adsorbent was synthesized using finely ground opoka and CaO. The molar ratio of calcium oxide and silicon dioxide was fixed at 1.5 by adding CaO. The required amounts of primary compounds, including 21.83 g of CaO and 38.17 g of opoka, were weighed and placed in a sealed plastic container with four porcelain grinding bodies. The mixture was then mixed for 45 min at 49 rpm using a Turbula Type T2F homogenizer (Artisan Technology Group, Czech Republic). After this procedure, 60 *g* of the initial material mixture and 600 ml of distilled water were combined (w/s ratio of 10) in a 1 L stainless steel autoclave ("Parr Instruments," Germany). Hydrothermal synthesis was conducted in unstirred suspensions at 200 °C for 16 h of isothermal curing. Afterward, the autoclave was quenched to room temperature. The suspensions were filtered, dried for 24 h at 50 ± 5 °C, and sieved through an 80 μm mesh sieve.

After hydrothermal synthesis, two crystalline calcium silicate hydrates (α-C_2SH [$2CaO·SiO_2·H_2O$] and tobermorite [$Ca_5Si_6O_{16}(OH)_2·4H_2O$]) with good adsorption properties were predominant in XRD (Fig. 2, a). Both materials have a porous structure (Dambrauskas et al., 2019; Tang et al., 2021) and a high calcium content, which allows them to adsorb phosphorus from the liquid medium effectively.

STA confirmed the XRD results. The first endothermic effect at 110 °C indicated the partial dehydration of calcium silicate hydrates and the removal of adsorbed water. The decomposition of the target compound (α-C_2SH) and unreacted portlandite occurred within a temperature range of 430–490 °C. At higher temperature ranges (650–750 °C), the sample showed a broad endothermic effect and lost 6.58% of its mass. The dehydration of calcium silicate hydrates is likely responsible for mass losses up to around 680 °C. In contrast, the decomposition of calcium carbonate into calcium oxide and carbon dioxide results in mass loss at higher temperatures. Finally, the recrystallization of calcium silicate hydrates into wollastonite can be attributed to an intense exothermic reaction around 855 °C.

Calculations of the nitrogen adsorption-desorption isotherms at 77 K showed that the specific surface area (S_{BET}) of the synthetic adsorbent was equal to 47.80 m^2/g, while the total pore volume ($\sum V_p$) was 0.193 cm^3/g. The obtained values are comparable with those presented in the literature (S_{BET} – 2–500 m^2/g; $\sum V_p$ – 0.05–0.3 cm^3/g) (Barrero et al., 2021; Dambrauskas et al., 2019; Siauciunas et al., 2021).

Scanning electron microscopy images of the adsorbent reveal particles of varying sizes and shapes (Fig. 1, c). Most particles exhibit plate-like and needle-like structures, indicating the formation of calcium silicate hydrates (tobermorite and α-C_2SH) with an ordered particle structure. The average particle size is small (<2 μm), ensuring a high probability of particle-liquid contact during the experiments. TEM analysis showed that the adsorbent consists of thin CSH nanosheet crystallites that tend to aggregate into a silicate network (Fig. 1, d). Although in the sample, some rods and shapeless crystallites were also present.

2.4. Adsorption experiments

Adsorption experiments were carried out in a Julabo PURA 10 thermostat at 25 °C, 35 °C, and 45 °C. One liter of KH_2PO_4 solution containing 0.2, 0.5, 1.0, 1.5, 2.6, or 5.0 g P^{5+}/L of phosphorus was mixed with 10 g of the adsorbent to perform the adsorption process. During the process, 10-mL liquid samples were collected at the following intervals: 30 s, 1 min, 3 min, 5 min, 10 min, 15 min, 30 min, and 1 h. After the first hour, samples were taken less frequently: at 3 h, 5 h, 8 h, 24 h, 48 h, 72 h, and 1 week. Following adsorption, the adsorbent was filtered and dried for 24 h at 50 ± 5 °C.

2.5. Adsorption kinetic models

Response surface methodology (Myers et al., 2016) was applied to determine optimal technological parameters (initial phosphorus ion

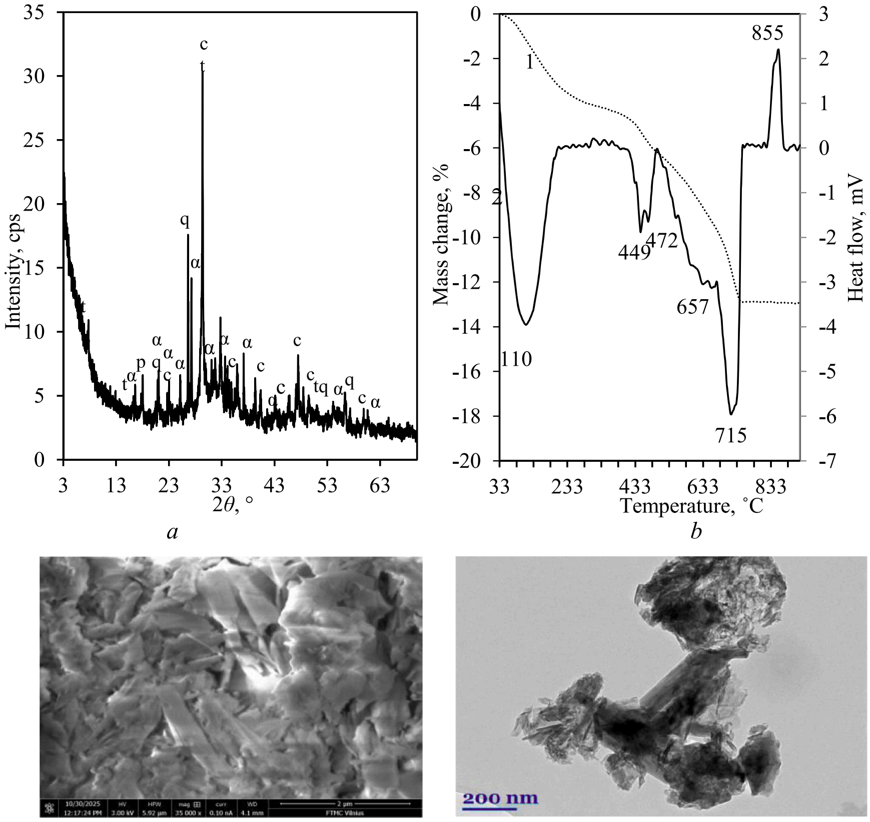

a
b
c
d

Fig. 1. XRD pattern (a), STA curves (b, 1 – TGA, 2 – DSC), SEM (c), and TEM (d) images of the synthetic adsorbent. Indexes: α – α-C_2SH, c – calcite, t – tobermorite, q – quartz, l – calcium aluminum silicate hydrate.

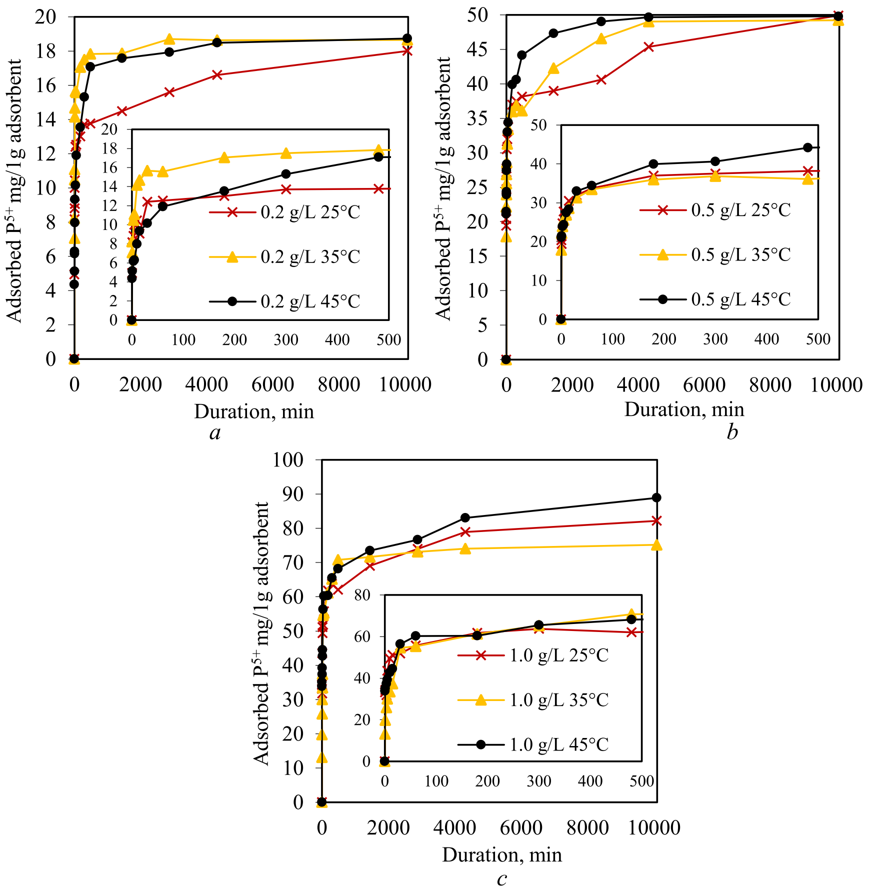

Fig. 2. An integral kinetic curve for phosphorus ion adsorption on a synthetic adsorbent.

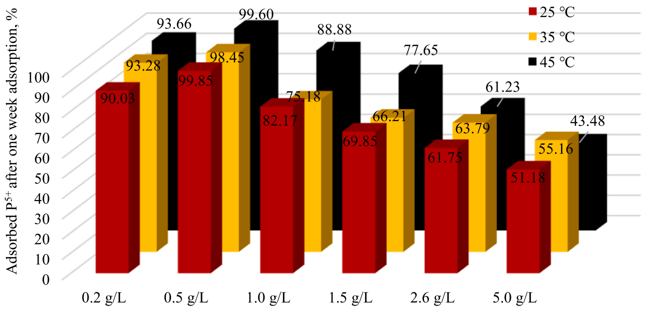

Fig. 3. Efficiency of phosphorus removal through adsorption by a synthetic adsorbent.

concentration and adsorption temperature) that maximize adsorption rate and/or minimize adsorption time. A second-order polynomial model was used to approximate the response surfaces over the investigated ranges of the phosphorus ions' initial concentration and the process temperature:

$$Y = \exp\ (a_0 + a_1\cdot x_1 + a_2\cdot x_2 + a_{11}\cdot x_1^2 + a_{22}\cdot x_2^2 + a_{12}\cdot x_1\cdot x_2; \tag{2}$$

where Y is the adsorption rate or the adsorption duration, x_1 is the initial concentration of phosphorus ions, x_2 is the temperature of the adsorption process, a_0, … a_{12} are the model parameters identified using data of a relevant factorial experiment.

The equilibrium data were used to evaluate pseudo-first-order and pseudo-second-order kinetic models to elucidate the mechanism of phosphorus adsorption on the synthesized adsorbent. The *pseudo-first-order* adsorption kinetics model was chosen, analogous to the Largergren model and described by Eq. (3) (Tan et al., 2017):

$$\frac{dq_t}{dt} = k_1\cdot(q_e - q_t); \tag{3}$$

Where q_e and q_t are the amounts of adsorbed ions at equilibrium, and at time t_e, respectively, (mg/g), k_1 is the rate constant of pseudo-first-order adsorption.

The *pseudo-second-order* adsorption kinetic model was chosen for further analysis and was calculated using the following equation (Tan et al., 2017):

$$\frac{dq_t}{dt} = k_2\cdot(q_e - q_t)^2; \tag{4}$$

Where $k_2$is the rate constant of the pseudo-second-order adsorption (g/mg·min).

After integration and applying the following conditions $t_0 = 0$ to $t = t_e$ and $q_t = 0$ to $q_t = q_e$, the integrated form becomes linear. The linearized forms of the pseudo-first-order and pseudo-second-order models are shown in Eqs. (5) and (6), respectively, as follows:

$$\log(q_e - q_t) = \log q_e - \frac{k_1}{2.303}\cdot t; \tag{5}$$

$$\frac{t}{q_t} = \frac{1}{kq_e^2} + \frac{1}{q_e}\cdot t; \tag{6}$$

The experimental data on adsorption equilibrium were analyzed using various isotherm equations, including the Langmuir, Freundlich, Temkin, and Dubinin-Radushkevich models. The Langmuir model assumes that each active center on a homogeneous surface is occupied by a single molecule, with the adsorption energy of that molecule constant and independent of surface coverage (Aigbe et al., 2021; Moussavi et al.,

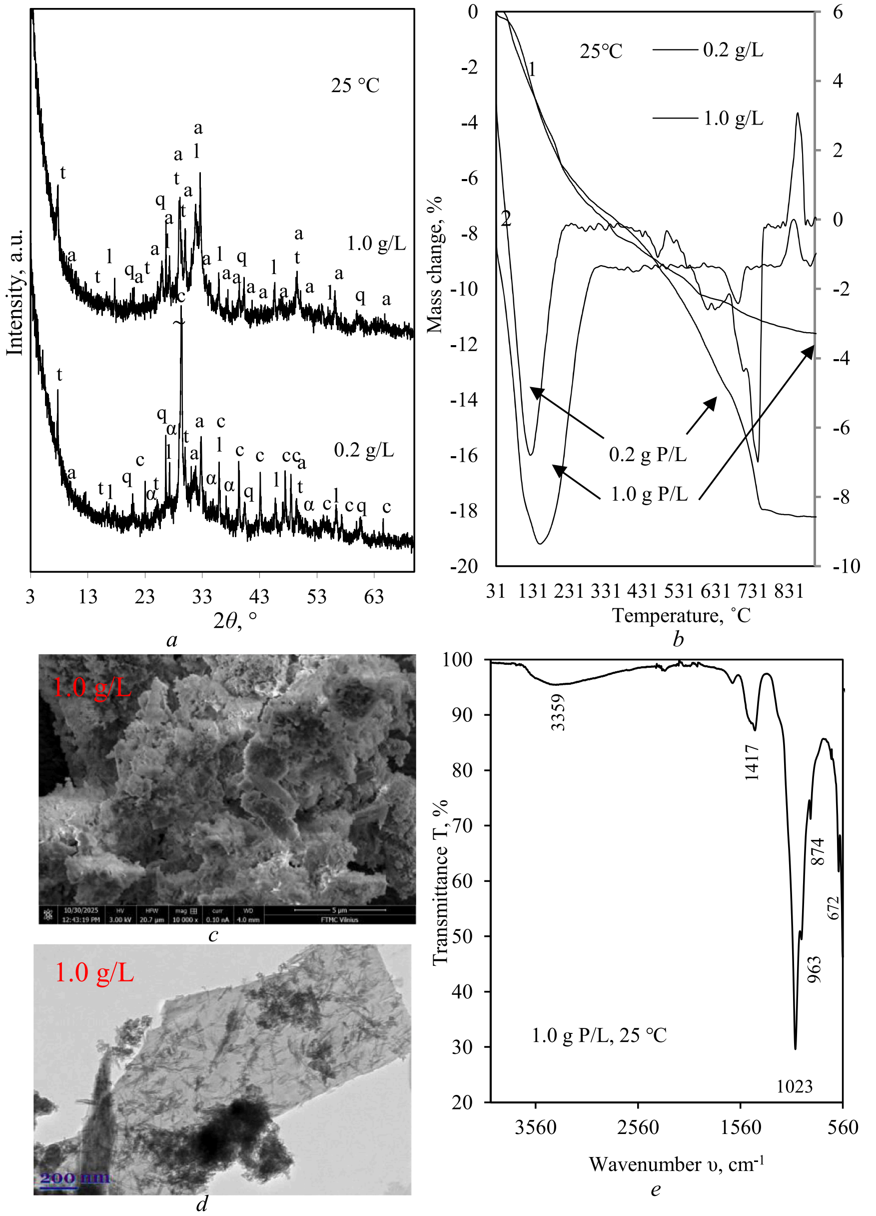

Fig. 4. XRD patterns (a), STA curves (b, 1 – TGA, 2 – DSC), SEM (c), TEM (d) images, and FT-IR spectra (e) of the adsorbent after one week of adsorption. Indexes: t – tobermorite, α – α-C_2SH, a – hydroxyapatite, q – quartz, l – calcium aluminum silicate hydrate.

2010; Sun et al., 2022).

$$q_e = q_m \frac{K_L C_e}{1 + K_L C_e}; \tag{7}$$

Where q_e and C_e are the concentrations at equilibrium in the solid (mol/g) and liquid (mol/l) phases, respectively; q_m is the Langmuir equation's equilibrium constant for adsorption capacity (mol/g); K_L is the constant at equilibrium (L/mol).

The Freundlich adsorption model is used as an alternative to the Langmuir model. This model assumes that adsorption occurs on a heterogeneous surface with a non-uniform distribution of adsorption energies, which tend to decrease logarithmically as the surface becomes more filled (Aigbe et al., 2021; Moussavi et al., 2010; Sun et al., 2022).

$$q_e = K_F C_e^{\frac{1}{n}}; \tag{8}$$

where K_F and n are the constants in the Freundlich equation representing the adsorption capacity and the intensity of the adsorption process.

The Temkin model is based on assumptions similar to those of the Freundlich model. However, it suggests that the decrease in adsorption energy is linear rather than logarithmic and is evenly distributed (Aigbe et al., 2021; Moussavi et al., 2010; Sun et al., 2022).

$$q_e = \frac{RT}{\Delta Q} \ln(K_T C_e); \tag{9}$$

where ΔQ and K_T are the constants in the Temkin equation related to heat adsorption (J/mol) and the equilibrium constant.

The *Dubinin-Radushkevich* model is based on potential energy theory and adsorption on a heterogeneous surface (Aigbe et al., 2021; Moussavi et al., 2010; Sun et al., 2022):

$$q_e = q_m exp\left[- \frac{\left(RTln\left(1 + \frac{1}{C_e}\right)\right)^2}{2E^2} \right]; \tag{10}$$

Table 1
Calculated parameters of the spent adsorbent (1 g P^{5+}/L, 25 °C) specific surface area (S_{BET}).

BET equation constants		Capacity of mono-layer X_m	S_{BET}, m^2/g	C_{BET} constant	Reliability coefficient, R^2	Total pore volume, cm^3/g
Slope $S = tga$	Intercept I					
43.17	0.35	0.02	80.06	122.79	1	0.388

where q_m and E are the maximum adsorption capacity (mol/g) and adsorption energy (J/mol), R is the gas constant (J/mol-K) and T is the absolute temperature (K).

The validity of these models was confirmed using experimental data in the linear forms of the relevant equations and by estimating their reliability coefficients (R^2).

3. Results and discussion

To assess the adsorption capacity and kinetics, the adsorption of phosphorus on the synthetic adsorbent was tested in solutions with phosphorus ion concentrations of 0.2, 0.5, 1.0, 1.5, 2.6, and 5.0 g P^{5+}/L. To better illustrate the data, the results were divided into two sections: the first covering lower-concentration solutions (0.1–1.0 g P^{5+}/L) and the second covering higher-concentration solutions (1.5–5.0 g P^{5+}/L). Finally, the results of kinetic and mathematical modeling are presented.

3.1. Adsorption of phosphorus on a synthetic adsorbent

3.1.1. Adsorption of phosphorus from solutions with a concentration of 0.2–1.0 g P^{5+}/L

In the solution with the lowest phosphorus concentration (0.2 g P^{5+}/L), the adsorbent adsorbed up to 10% of the initial amount at the beginning of the process (Fig. 2, a). After 15 min of adsorption, the removal efficiency reached approximately 50%, or 9.07 mg P^{5+}/g. As the adsorption duration was extended, the amount of adsorbed phosphorus increased, and after one week of the experiments, the phosphorus adsorption result was 18.01 mg P^{5+}/g. It was found that increasing the liquid medium temperature to 35 °C or 45 °C significantly influenced the initial stage of the process. However, after one week, the amount of adsorbed phosphorus was similar across all temperatures. Overall efficiency slightly improved with temperature increases from 25 °C to 45 °C (Fig. 3).

The adsorption process was also studied at a higher initial phosphorus concentration of 0.5 g P^{5+}/L (Fig. 2, b). The adsorbent exhibited similar behavior in the initial stage, removing over 50% of phosphorus within five minutes. Prolonging the experiment to 5 h led to intensive adsorption, reaching a capacity of 33.72 mg P^{5+}/g. After this rapid phase, a slower adsorption continued, during which the adsorbent absorbed an additional ~16 mg P^{5+}/g over 160 h. Increasing the temperature to 35–45 °C enhanced the initial adsorption rate, but after one week, the final adsorption efficiency became temperature-independent and exceeded 98% (Fig. 3).

Slightly different results were observed in the solution containing 1 g P^{5+}/L (Fig. 2, c). In this case, the adsorption again showed a rapid initial phase, with >50% adsorption efficiency achieved within 15–30 min, regardless of temperature. However, after one week of adsorption at 25 °C, the efficiency was only 82.17% (or 82.17 mg P^{5+}/g) (Fig. 3). Even lower efficiency (~75%) was reached after adsorption at 35 °C. Better results were observed at 45 °C, where the adsorbent removed >88% of the phosphorus present in the liquid medium.

Thus, the synthetic adsorbent experienced a rapid initial adsorption phase that slowed after 15–30 min. Following this quick interaction, a slower adsorption period occurred. The synthetic adsorbent demonstrated the highest phosphorus removal efficiency (75–99%) in solutions with phosphorus concentrations below 1 g P^{5+}/L (Fig. 3).

Table 2
Kinetic parameters of pseudo-first and pseudo-second order for phosphorus ion adsorption at different temperatures.

Initial phosphorus concentration	Temperature	R^2	$q_{e(exp)}$ (mg/g)	$q_{e(cal)}$ (mg/g)	k_1 (g/(mg·min))	k_2 (g/(mg·min))
0.2 g P^{5+}/L				Pseudo-first-order kinetic model		
	25 °C	0.7699	18.656	7.222	–	–
	35 °C	0.8149	18.723	4.378	–	–
	45 °C	0.8902	18.656	7.739	–	–
				Pseudo-second-order kinetic model		
	25 °C	0.9997	18.007	16.275	–	0.00186
	35 °C	0.9998	18.656	18.626	–	0.00493
	45 °C	0.9998	18.723	18.383	–	0.00189
0.5 g P^{5+}/L				Pseudo-first-order kinetic model		
	25 °C	0.9486	48.787	18.828	–	–
	35 °C	0.7587	49.223	23.304	–	–
	45 °C	0.9538	49.798	18.986	–	–
				Pseudo-second-order kinetic model		
	25 °C	0.9986	48.787	43.811	–	0.000696
	35 °C	0.9988	49.223	48.396	–	0.000387
	45 °C	0.9984	49.798	49.607	–	0.000756
1.0 g P^{5+}/L				Pseudo-first-order kinetic model		
	25 °C	0.8733	82.168	33.152	–	–
	35 °C	0.7401	75.179	27.063	–	–
	45 °C	0.8269	88.876	38.944	–	–
				Pseudo-second-order kinetic model		
	25 °C	0.9986	82.168	81.643	–	0.000182
	35 °C	0.9999	75.179	75.102	–	0.000508
	45 °C	0.9974	88.876	87.844	–	0.000137

$\Sigma q_{e(exp)}$ represents the equilibrium adsorption capacity, mg/g, obtained from data of experiments; $\Sigma q_{e(exp)}$ is the equilibrium adsorption capacity, mg/g, derived by employing kinetic models; $\Delta\Sigma q_e$ represents the difference between $\Sigma q_{e(exp)}$ and $\Sigma q_{e(exp)}$, %; k_1 is the adsorption rate constant calculated by using pseudo-firs-order kinetic model, min^{-1}; k_2 is the adsorption rate constant calculated by using pseudo-second-order kinetic model, g/(mg·min).

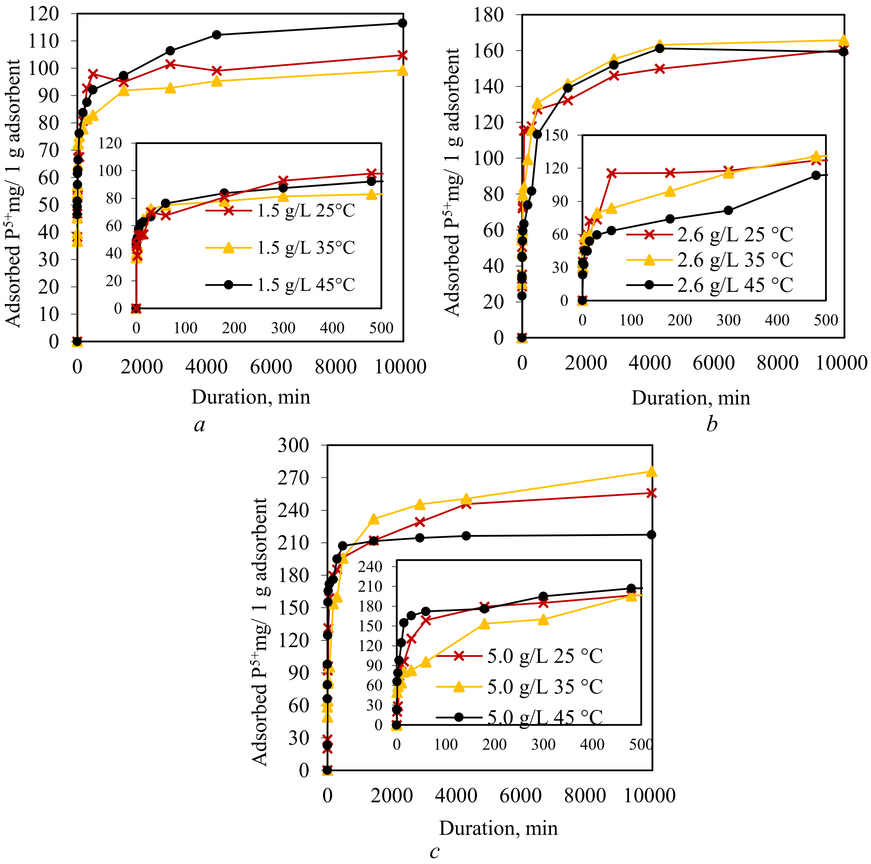

a

b

c

Fig. 5. Kinetic curves illustrating the adsorption of phosphorus ions on a synthetic adsorbent.

3.1.2. Stability of the adsorbent during adsorption from solutions with a concentration of 0.2–1.0 g P^{5+}/L

To understand how adsorbed phosphorus ions influence the structure of the synthetic adsorbent and assess the stability of the materials, the product after 1 week of adsorption was analyzed using XRD and STA.

XRD analysis revealed a strong chemical interaction between the calcium silicate hydrates (α-C_2SH and semi-crystalline CSH) present in the adsorbent and phosphorus ions during the adsorption experiment (Fig. 4, a and Fig. S1, a). This interaction resulted in the formation of hydroxyapatite ($Ca_{10}(PO_4)_6(OH)_2$). The intensity of hydroxyapatite diffraction peaks increased with higher phosphorus concentration and adsorption temperature. (Fig. 4, a and Fig. S1, a). Additionally, α-C_2SH showed complete reactivity after adsorption in solutions with phosphorus concentrations above 0.5 g P^{5+}/L. Other phases in the synthetic adsorbent's structure (tobermorite, quartz, and calcium aluminum silicate) remained stable, although their diffraction peak intensities varied slightly with changes in adsorption process parameters, such as concentration and temperature. Thus, high-basicity calcium silicates hydrates (α-C_2SH) chemically reacted with phosphorous ions, forming hydroxyapatite, while low-basicity calcium silicates hydrates (tobermorite) acted as adsorbents.

The findings from the XRD analysis were consistent with the STA data (Fig. 4, b and Fig. S1, b). The DSC curve exhibited a typical thermogravimetric response, with the most significant mass loss up to 200 °C caused by the removal of free, adsorbed, and interlayer water from the CSH structure. The TGA showed that this mass loss decreased with increasing adsorption temperature, indicating that less water was adsorbed at higher temperatures. An endothermic effect at around 470 °C was linked to the decomposition of portlandite and/or α-C_2SH. This effect was observed in samples after adsorption in the solution with the lowest phosphorus concentration (0.2 g P^{5+}/L). Other spent-adsorbent samples did not display this thermal effect, confirming that α-C_2SH reacted with phosphorus ions to form hydroxyapatite.

An endothermic effect occurring at 500–650 °C can be attributed to the dehydration of calcium phosphates, calcium silicate hydrates, or the decomposition of low-crystallinity carbonates. This effect was observed only in the adsorbent after adsorption at 25 °C with an initial phosphorus concentration of 0.2 g P^{5+}/L. A similar effect was observed in the synthetic adsorbent (Fig. 1, b). Therefore, higher concentrations of phosphorus ions and increased temperature caused significant structural changes. An endothermic effect around 750–800 °C indicates that calcium carbonate decomposes into CaO and CO_2. The heat of this effect and the associated mass loss due to carbonate decomposition were similar in spent adsorbents obtained after sorption from solutions containing 0.2–0.5 g P^{5+}/L. However, increasing the concentration to 1.0 g P^{5+}/L resulted in a decrease in mass loss of about 0.52% and a reduction in the heat of effect to 12.31 J/g. This indicates that calcium carbonate becomes metastable and reacts with phosphorus at the highest P^{5+} concentrations.

Ultimately, the DSC curves of each sample showed an exothermic effect around 860 °C, indicating CSH recrystallization into wollastonite. The area of this effect decreased as the initial phosphorus concentration increased from 0.2 to 0.5 g P^{5+}/L to 1.0 g P^{5+}/L, confirming the reduced amount of calcium silicate hydrates in the spent adsorbent.

To investigate the functional groups formed during adsorption, the samples after adsorption were analyzed by FT-IR (Fig. 4, e). For this analysis, the sample obtained after adsorption in the solution with an initial concentration of 1 g P^{5+}/L was used. The broad band between 3750 and 3000 cm^{-1} corresponds to the stretching mode of the absorbed water. The absorption bands characteristic of calcite were observed at 874 cm^{-1} and 1417 cm^{-1}, confirming XRD and STA results (Fig. 4). Unfortunately, the absorption bands characteristic of PO_4^{3-} group from phosphates and Si-O-Si or O-Si-O groups from silicates overlapped in the higher frequency range (560–1100 cm^{-1}).

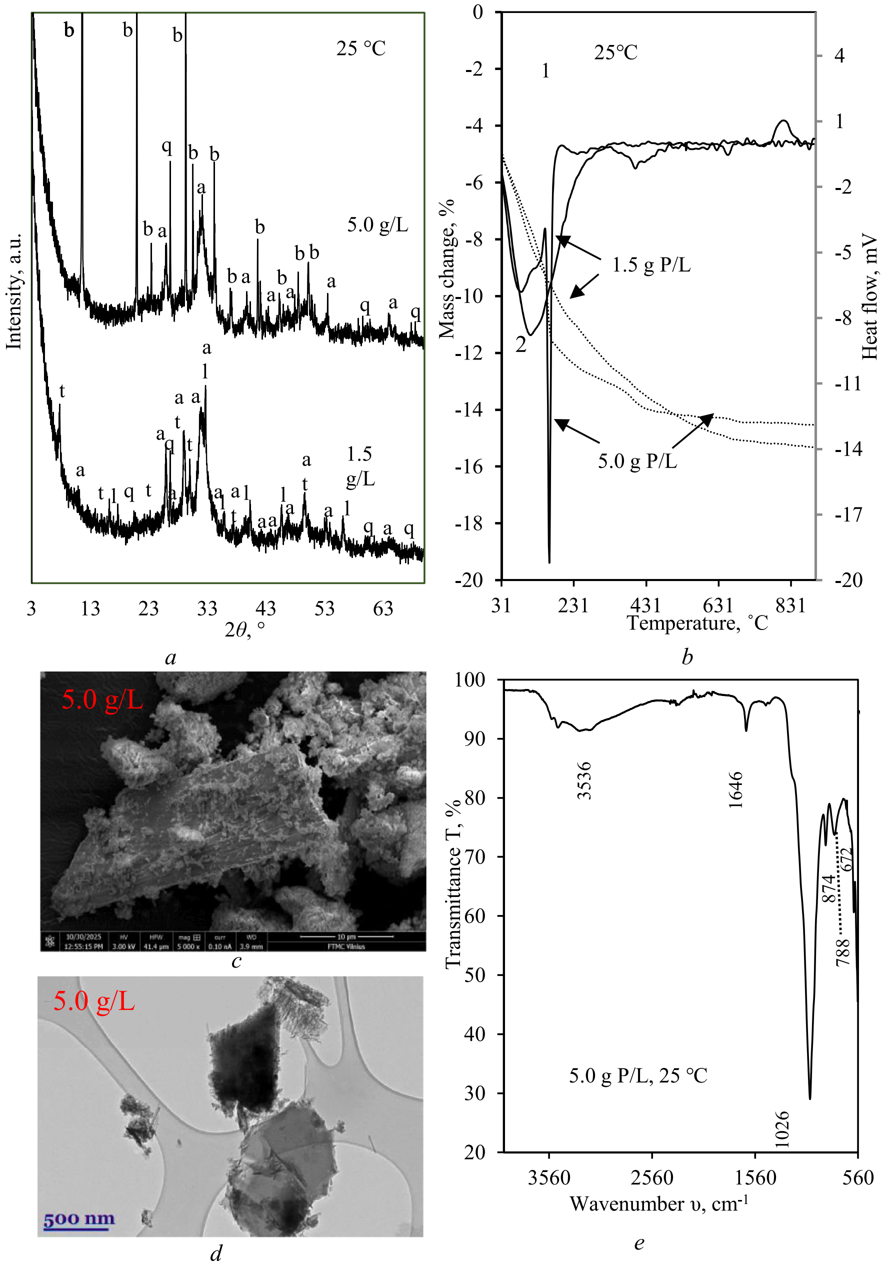

Fig. 6. XRD patterns (a), STA curves (b, 1 – TGA, 2 – DSC), SEM (c), TEM (d) images, and FT-IR spectra (e) of the adsorbent after one week of adsorption. Indexes: t – tobermorite, α – α-C_2SH, a – hydroxyapatite, q – quartz, l – calcium aluminum silicate hydrate, b – brushite.

The results of nitrogen adsorption showed that after adsorption (1 g P^{5+}/L, 25 °C), the specific surface area of spent adsorbent significantly increased from 47.80 m^2/g (before adsorption) to 80.06 m^2/g (Table 1). Meanwhile, the total pore volume ($\sum V_p$) increased from 0.193 cm^3/g to 0.388cm^3/g.

SEM and TEM images showed that adsorption strongly affected the morphology of the samples (Fig. 1, c and Fig. 4, c, d). During adsorption (1 g P^{5+}/L, 25 °C), the shape of particles changed from plate-like and needle-like with an average size of ~2 µm (Fig. 1, c) to uniform particles with a size of 0.2 µm up to 5 µm (Fig. 4, c). The decrease in particle size led to increases in S_{BET} and $\sum V_p$. Meanwhile, TEM images showed that thin CSH nanosheet crystallites were still present in the sample; however, small, uniform, needle-shaped crystallites (diameters of 5–10 nm and lengths of 150–200 nm) were also detected (Fig. 4, d). These crystallites can be related to the formation of new crystalline compounds (hydroxyapatite) during adsorption.

Table 3
Calculated parameters of the spent adsorbent (5 g/L, 25 °C) specific surface area (S_{BET}).

BET equation constants		Capacity of mono-layer X_m	S_{BET}, m^2/g	C_{BET} constant	Reliability coefficient, R^2	Total pore volume, cm^3/g
Slope S=tga	Intercept I					
48.54	0.63	0.02	70.87	77.87	1	0.259

3.1.3. Kinetics of adsorption from solutions with concentration 0.2–1.0 g P^{5+}/L

Kinetic equations are crucial for understanding adsorption behavior, measuring adsorption rates, and optimizing experimental conditions. To address this, pseudo-first-order and pseudo-second-order kinetic models were used to determine the kinetic parameters of phosphorus ion adsorption on the synthetic adsorbent.

The coefficient of determination (R^2) was calculated, and the calculated equilibrium concentration values ($\Sigma q_{e(cal)}$) were compared with the experimental concentration values ($\Sigma qe_{(exp)}$) to assess the model's suitability for the adsorption process. If the errors between estimated and experimental equilibrium concentrations were <10% and the R^2 values ranged from 0.95 to 1.00, the model was considered valid.

Table 2 and Figure S2 summarize the results of fitting the experimental data to pseudo-first-order and pseudo-second-order kinetic model equations. It was observed that the pseudo-first-order kinetic model did not fit the experimental data for several reasons. Linear dependence was not evident; the coefficients of determination (R^2) for the linear fit of the regression curves to the experimental data were lower than 0.90 (Fig. S2, and Table 2). As shown in Table 2, there was a significant difference between the calculated values and the experimentally obtained values.

In contrast, the pseudo-second-order model provided a suitable framework for characterizing the adsorption process, with an R^2 value of 0.99 (Fig. 6, d, e, f). Additionally, the differences between $\Sigma q_{e(exp)}$ and $\Sigma q_{e(cal)}$ were found to be insignificant (<2%) (Table 2). The data from the adsorption experiment at 25 °C with an initial phosphorus concentration of 0.2 g P^{5+}/L showed a more notable difference (about 10%) between the calculated and experimental results. The adsorption rate constant, represented by the k_2 coefficient, reached its maximum at a concentration of 0.2 g P^{5+}/L and decreased with increasing phosphorus concentration. Adsorption in solutions with 0.5 g P^{5+}/L or 1.0 g P^{5+}/L was characterized by a k_2 value of 0.0002–0.0007 (g/(mg·min)).

The suitability of the pseudo-second-order kinetic model for phosphorus adsorption onto the synthesized adsorbent indicates that multiple mechanisms, including chemical interactions and electrostatic attraction of phosphorus ions with reactive centers on calcium silicate hydrate surfaces, are involved. These results suggest that the adsorption efficiency may be influenced by a higher driving force, which encourages the faster transfer of phosphorus onto the adsorbent surface, along with the availability of exposed surface area and remaining active sites. These findings align with the XRD data, which proved that a chemical interaction between the adsorbent and phosphorus ions occurred.

3.1.4. Adsorption of phosphorus from solutions with concentration 1.5–5.0 g P^{5+}/L

The initial phosphorus concentration was increased to examine its impact on adsorption behavior. A higher phosphorus concentration in the liquid medium, ranging from 1.5 to 5.0 g P^{5+}/L, influenced the amount of phosphorus ions adsorbed and the adsorption efficiency, but it did not alter the overall process trend (Figs. 3 and 5).

The adsorption kinetic curves obtained during the process in solutions with higher phosphorus concentrations (1.5–5.0 g P^{5+}/L) showed similar tendency of process including slight dependence on temperature (Fig. 5). The synthetic adsorbent rapidly absorbed phosphorus ions from the liquid medium at the beginning of the process (up to 10 min), reaching phosphorus intercalation levels of up to 50 mg P^{5+}/g. The adsorption proceeded intensively up to 10 h, leading to an increase in adsorbed phosphorus to 80–100 mg P^{5+}/g, 100–125 mg P^{5+}/g, and 200–210 mg P^{5+}/g as the initial phosphorus concentrations increased from 1.5 g P^{5+}/L to 2.6 g P^{5+}/L and 5.0 g P^{5+}/L, respectively. At the end of the process (after 1 week), the adsorbent absorbed 100–115 mg P^{5+}/g in solutions with an initial phosphorus concentration of 1.5 g P^{5+}/L. In this case, the phosphorus removal efficiency was 66–77% (Fig. 3). Increasing the initial phosphorus concentration to 2.6 g P^{5+}/L and 5.0 g P^{5+}/L resulted in higher phosphorus adsorption capacity, reaching 159–166 mg P^{5+}/g and 217–276 mg P^{5+}/g, respectively. However, the removal efficiency was only 61–64% in solutions with 2.6 g P^{5+}/L and 43–55% in solutions with 5.0 g P^{5+}/L. Consequently, elevated concentrations led to increased phosphorus intercalation into the adsorbent structure, concurrently diminishing removal efficiency.

3.1.5. Stability of the adsorbent during adsorption from solutions with a concentration of 1.5–5.0 g P^{5+}/L

The mineralogical composition analysis of XRD showed that increasing the phosphorus ion concentration in the liquid medium from 1.0 g P^{5+}/L to 1.5 g P^{5+}/L and 2.6 g P^{5+}/L did not alter the interaction between the adsorbent and phosphorus ions. Specifically, phosphorus ions reacted with α-C_2SH and semi-crystalline calcium silicate hydrates (present in the adsorbent's structure), leading to the formation of

Table 4

Pseudo-first- and pseudo-second- order kinetic parameters for phosphorus ions adsorption at different temperatures.

Initial phosphorus concentration	Temperature	R^2	$q_{e(exp)}$ (mg/g)	$q_{e(cal)}$ (mg/g)	k_1 (g/(mg·min))	k_2 (g/(mg·min))
1.5 g P^{5+}/L			Pseudo-first-order kinetic model			
	25 °C	0.6119	104.779	35.697	–	–
	35 °C	0.7630	99.312	34.094	–	–
	45 °C	0.9064	116.475	50.043	–	–
			Pseudo-second-order kinetic model			
	25 °C	0.9994	104.779	104.109	–	0.00025
	35 °C	0.9994	99.312	98.752	–	0.00023
	45 °C	0.9988	116.475	115.868	–	0.00013
2.6 g P^{5+}/L			Pseudo-first-order kinetic model			
	25 °C	0.7608	160.559	78.467	–	–
	35 °C	0.9415	165.850	95.173	–	–
	45 °C	0.9388	159.194	121.492	–	–
			Pseudo-second-order kinetic model			
	25 °C	0.9983	160.559	159.101	–	0.000083
	35 °C	0.9992	165.850	165.909	–	0.000085
	45 °C	0.9988	159.194	160.325	–	0.000066
5 g P^{5+}/L			Pseudo-first-order kinetic model			
	25 °C	0.8187	255.897	143.608	–	–
	35 °C	0.8316	275.798	178.358	–	–
	45 °C	0.7946	217.394	67.672	–	–
			Pseudo-second-order kinetic model			
	25 °C	0.9860	255.897	258.650	–	0.000021
	35 °C	0.9839	275.798	278.044	–	0.000016
	45 °C	1.0000	217.394	217.470	–	0.000026

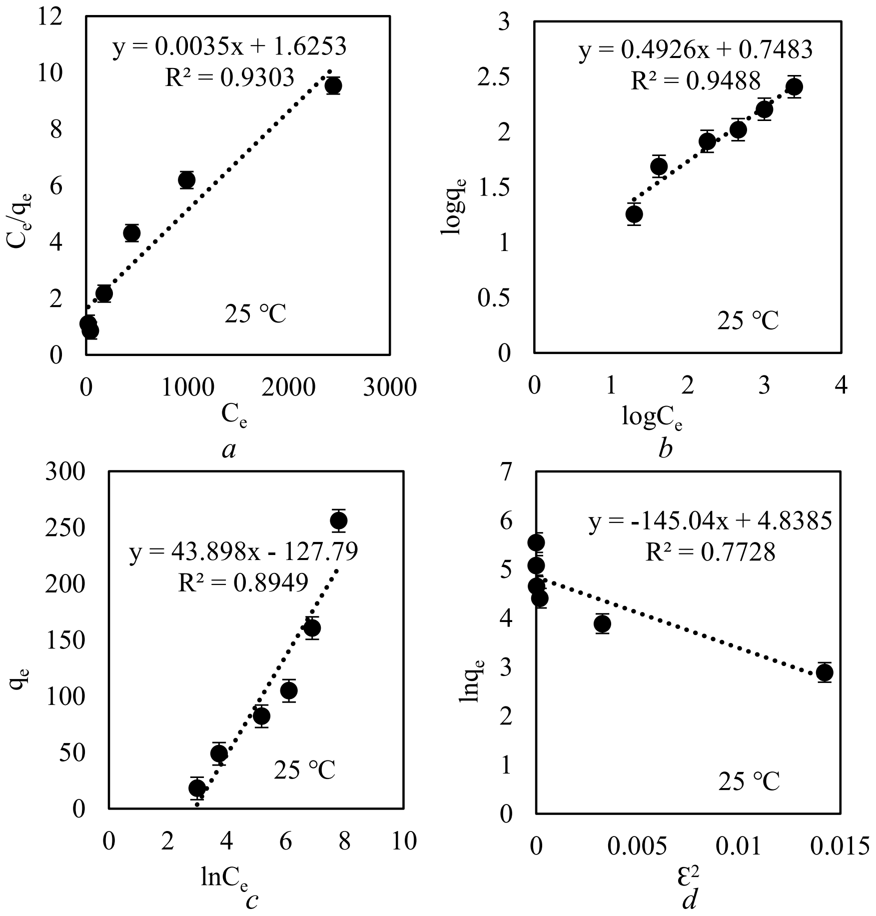

Fig. 7. Langmuir (a), Freundlich (b), Temkin (c), and Dubinin-Radushkevich (d) adsorption isotherms.

Table 5
The parameters of Langmuir, Freundlich, Temkin and Dubinin-Radushkevich adsorption isotherms.

Adsorption isotherm	Parameter	25 °C	35 °C	45 °C
Langmuir	q, mg/g	208.333	151.515	196.078
	K_L, L/mg	1.625	2.987	1.617
	R_L	0.003	0.002	0.003
	R^2	0.930	0.828	0.987
Freundlich	K_F	2.113	2.236	2.661
	$1/n$	0.493	0.472	0.415
	R^2	0.949	0.954	0.922
Temkin	K_T, L/mg	18.376	15.577	8.451
	b_T, kJ/mol	56.428	58.159	70.768
	R^2	0.895	0.791	0.983
D-R	$q_{D\text{-}R}$, mg/g	126.280	125.286	130.061
	$B_{D\text{-}R}$, mol^2/kJ^2	145.040	65.900	59.927
	E, kJ/mol	0.059	0.087	0.091
	R^2	0.773	0.727	0.851

hydroxyapatite (Fig. S3 and Fig. 6). Other phases, including tobermorite, calcium aluminate silicate, and quartz, remained stable.

The obtained results were confirmed by STA data. The DSC showed only one endothermic effect and a small exothermic effect after the adsorption process in solutions with initial P^{5+} concentrations of 1.5 and 2.6 g P^{5+}/L (Fig. 6, b and Fig. S3, b). The first intensive endothermic effect (30–350 °C) can be assigned to the removal of adsorbed water and the dehydration of hydroxyapatite, tobermorite, and calcium aluminate silicate. It is worth mentioning that mass loss during this effect is almost two times higher in the spent adsorbent obtained after adsorption at 25 °C, compared to the sample obtained after adsorption at 45 °C. This suggests that the adsorbent's uptake capacity decreased with increasing experimental temperature, or that higher temperature led to greater hydrate decomposition. Also, a small exothermic effect (~840 °C) was noticed only in the sample obtained after sorption at 25 °C with an initial phosphorus concentration of 1.5 g P^{5+}/L. The absence of this exothermic effect in other samples confirmed that the semicrystalline calcium silicate hydrates were fully reacted with phosphorus ions, forming hydroxyapatite.

At an initial phosphorus concentration of 5 g P^{5+}/L, the high supersaturation of phosphorus ions in solution led to the formation of both brushite ($CaPO_3(OH)·2H_2O$) and hydroxyapatite at temperatures of 25 °C and 35 °C. According to the literature, brushite is calcium phosphate, which is stable at low temperatures; increasing temperature leads to dehydration or recrystallization into other calcium phosphates. For this reason, brushite was not detected in the sample obtained after adsorption at 45 °C. Also, under these adsorption conditions, tobermorite became metastable and reacted with phosphorus ions by forming calcium phosphates.

DSC analysis showed that the spent adsorbent after adsorption at 25 °C and 35 °C exhibited an intense endothermic effect at 193 °C (Fig. 6, b). This effect can be attributed to the dehydration of brushite and the formation of monetite, which recrystallized into calcium pyrophosphate in the temperature range 350–500 °C.

FT-IR spectra of the spent adsorbent confirmed XRD and STA results (Fig. 6, e). A large band between 3600 and 3000 cm^{-1} corresponds to the stretching mode of the absorbed water, whose intensity increased with the initial concentration of phosphorus in the solution. An intense absorption band at 1646 cm^{-1} is characteristic of δ-OH vibrations in the brushite structure. As in a previous case (Fig. 4, e), absorption bands characteristic of silicates and phosphates overlapped at 672 cm^{-1} and

Table 6
The experimental design matrix with the experimental values of the response variables - adsorption rate and duration.

No.	Experimental conditions				Experimental results	
	Phosphorus ion concentration (x_1)		Adsorption temperature (x_2)		Average adsorption rate1)	Adsorption duration2)
	Code values	Real values, g/L	Code values	Real values, °C	g/L/min	min
1	+1	5.0	+1	45	0.000581	4300
2	−1	0.2	+1	45	0.00476	21
3	+1	5.0	−1	25	0.000793	3470
4	−1	0.2	−1	25	0.0143	7
5	+1	5.0	0	35	0.00218	1260
6	−1	0.2	0	35	0.0333	3
7	0	2.6	+1	45	0.00112	1160
8	0	2.6	−1	25	0.00138	940
9	0	2.6	0	35	0.00247	526

1) Average adsorption rate is the ratio between 50% of the initial phosphorus ion concentration in the solution and the time during which the adsorbed phosphorus ion concentration in the adsorbent reaches 50% of the initial phosphorus ion concentration in the adsorption solution.
2) Adsorption duration is the time during which the adsorbed phosphorus ion concentration in the adsorbent reaches 50% of the initial phosphorus ion concentration in the adsorption solution.

1026 cm^{-1} (Fig. 6, e). However, a new absorption band at 788 cm^{-1} can be assigned to vibrations of structural water from brushite. Also, the disappearance of absorption bands at ~1417 cm^{-1} confirmed that calcium carbonate was not stable under these adsorption conditions.

It was calculated that, after adsorption (5 g P^{5+}/L, 25 °C), the specific surface area and total pore volume decreased to 70.87 m^2/g and 0.209 cm^3/g, respectively (Table 3). However, these values were still higher than those of the synthetic adsorbent. It is likely that calcium phosphates crystallized during adsorption increased the surface area and formed new pores.

It was found that an increased phosphorus concentration influenced not only surface properties but also particle morphology (Fig. 6, c and d). SEM analysis revealed plate-like particles with dimensions of approximately 10 μm in width and 20 μm in length, characteristic of dicalcium phosphate (brushite) (Fig. 6, c). Also, agglomerates of uniform particles are clearly visible in SEM micrographs. TEM analysis confirmed the SEM results, as large crystallites (0.5–1 μm) were detected, which can be assigned to brushite (Fig. 6, d). Also, some smaller crystallites can be seen in TEM micrographs, which may correspond to hydroxyapatite or other minor phases that are not distinguishable in the XRD pattern.

3.1.6. *Kinetics of adsorption from solutions with concentration 1.5–5.0 g P^{5+}/L*

The calculations of kinetic parameters using pseudo-first-order and pseudo-second-order kinetic equations showed that the pseudo-first-order model did not fit the adsorption process, as R^2 values ranged from 0.6 to 0.94 and there was a significant discrepancy between $q_{e(cal)}$ and $q_{e(exp)}$ (Table 4). Similar results were obtained during calculations for adsorption from solutions with P^{5+} concentrations of 0.2–1.0 g P^{5+}/L (Table 1).

The results showed that the pseudo-second-order model fit the experimental data better, as indicated by higher R^2 values (≥0.9983) (Figure S4). Additionally, there was a more precise alignment between calculated ($q_{e(cal)}$) and experimental ($q_{e(exp)}$) equilibrium adsorption capacities (Table 4).

The pseudo-second-order model describes the chemisorption process; therefore, it can be concluded that the adsorption of phosphorus ions on the synthetic adsorbent was a chemical process rather than physical. Additionally, the process did not depend on the initial phosphorus concentration or the liquid medium temperature, as the pseudo-second-order model fit the experimental data under all experimental conditions. These data confirm the chemical interaction between phosphorus and calcium silicate hydrates.

Adsorption kinetic calculation assumes that the adsorption rate constant (k_2) decreases with increasing initial phosphorus concentration, indicating slower adsorption at higher concentrations. In solutions with 1.5 g P^{5+}/L, k_2 ranged from 0.00025 to 0.00013 g/(mg·min), while in solutions with 5 g P^{5+}/L, it was significantly lower (from 0.000016 to 0.000026 g/(mg·min)). Therefore, increasing the initial phosphorus concentration led to higher phosphorus intercalation, but slower process kinetics.

3.2. *Modelling of adsorption isotherms*

To better understand the adsorption mechanism of phosphorus by the synthetic adsorbent, the adsorption models of Langmuir, Freundlich, Temkin, and Dubinin-Radushkevich were applied to the experimental data. The model results are shown in Fig. 7 and S5, with the corresponding parameters summarized in Table 5. The suitability of each model for the adsorption process was assessed by the coefficient of determination (R^2), which indicated how well the obtained data fit the regression line.

It was determined that temperature affected the adsorption mechanism. The calculations showed that the Langmuir and the Freundlich isotherm models described phosphorus adsorption quite well at 25 °C, as correlation coefficients ranged between 0.93 and 0.95 (Fig. 7). The Langmuir model is suitable for monolayer adsorption, while the Freundlich model suggests that adsorption occurs on a heterogeneous surface and is not limited to a single layer (i.e., the adsorption sites are filled with their entire volume). The Langmuir model is usually not suitable for describing chemical adsorption; however, the formation of stable Ca–P compounds on the surface may behave like a “monolayer”. The q value obtained from this model indicated a high adsorption capacity, while the R_L value was below 0.1, suggesting very favorable adsorption (Table 5). Meanwhile, the parameters of the Freundlich model indicated that the process is chemisorption ($1/n < 1$) and that the adsorbent has high adsorption capacity ($K_F > 1$). Also, the coexistence of different interaction mechanisms may result from the presence of multiple phases in the adsorbent structure – i.e., α-C_2SH acted as a chemisorbent, while tobermorite behaved more as a physical sorbent.

At 35 °C, the adsorption process was best described by the Freundlich model, as the R^2 value was closest to 1.0. Other models exhibited significantly lower values ($R^2 < 0.9$), indicating that they were not suitable for describing the process under these conditions. These results further support that chemisorption occurred on a heterogeneous surface at this temperature. The high K_F value also confirmed the adsorbent’s high capacity.

At 45 °C, both the Langmuir and Temkin isotherm models described the adsorption process well ($R^2 < 0.98$), while the Freundlich model showed a lower correlation ($R^2 \sim 0.92$). The Temkin isotherm model implies that the adsorption energy decreases linearly and is uniformly

Table 7
Identified parameter values for the adsorption rate and the duration prediction.

Predicted variable	a_0	a_1	a_2	a_{11}	a_{22}	a_{12}
Adsorption rate	−5.7393	−1.2869	−0.2700	0.8419	−1.0829	0.1972
Adsorption duration	6.0108	2.928	0.2539	−1.7648	1.0675	−0.2210

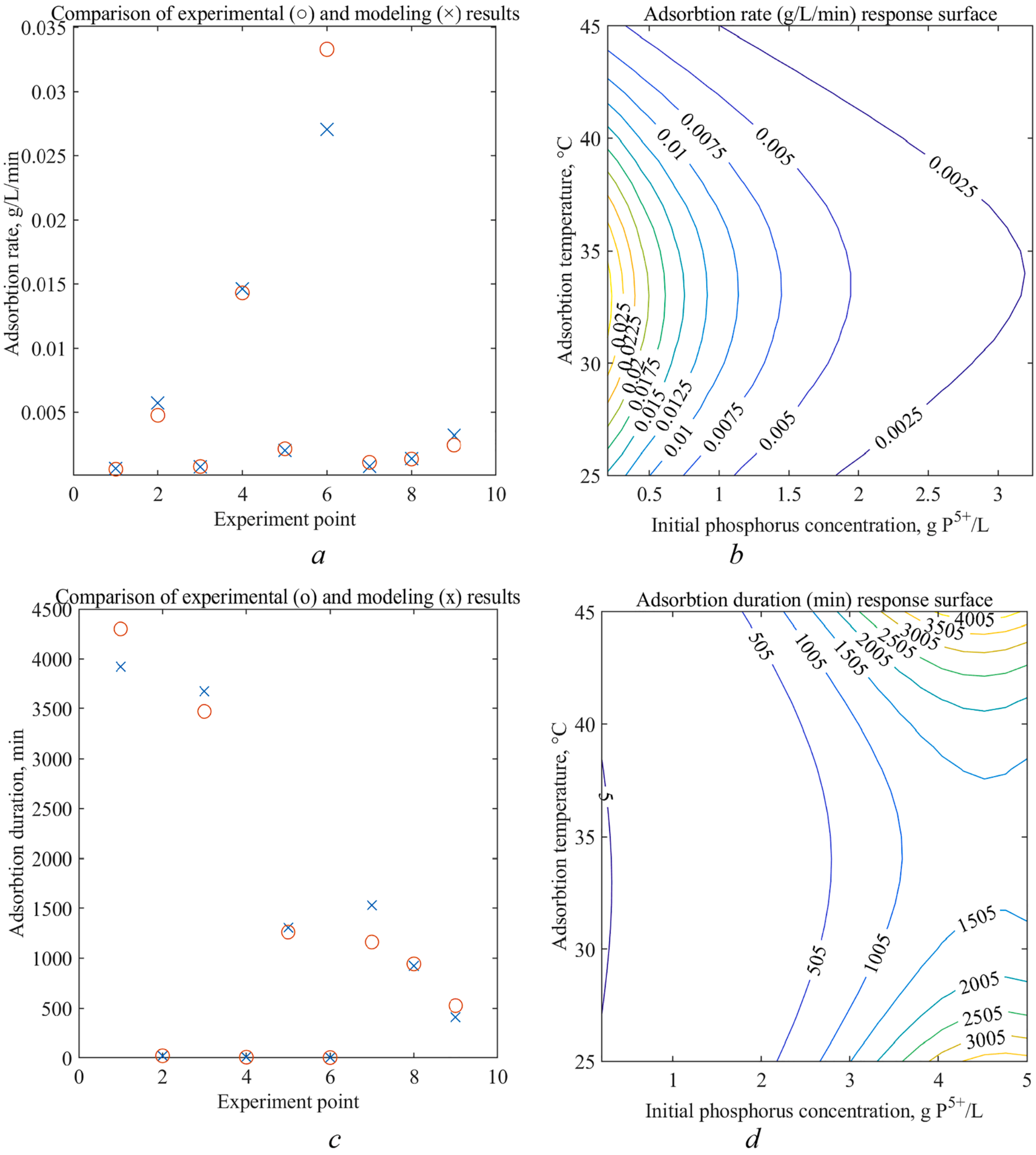

Fig. 8. Model predictions of experimental data (a, c) and model-based response surface plots of anticipated adsorption rate (b) and duration (d).

distributed across the surface.

It is worth noting that the Dubinin-Radushkevich model showed no linear dependence across all investigated temperatures, suggesting that van der Waals forces did not determine the adsorption mechanism on the adsorbent surface.

The combined analysis of the pseudo-first-order and pseudo-second-order kinetic equations, along with the adsorption isotherm models, allows to conclude that the adsorption of phosphorus by synthetic adsorbent was chemical in nature, controlled by different mechanisms depending on temperature and surface properties.

3.3. *Prediction of adsorption based on a response surface model*

The objective of the experiments was to investigate the influence of phosphorus ion concentration and adsorption temperature on adsorption efficiency, specifically on adsorption rate and duration. To estimate the response surfaces, an experimental plan based on a design close to the D-optimal (Kiefer) experimental design points was applied (Hartmann et al., 1974). The experimental design ranges for phosphorus ion concentration (x_1) and adsorption temperature (x_2) were selected based on previous experiments: $0.2 \leq x_1 \leq 5.0$ g P^{5+}/L, and $25 \leq x_2 \leq 45$ °C. The experimental design matrix and the corresponding experimental results are presented in Table 6.

In the information sources of experimental research design, the typical experimental design plans for typical polynomial models are commonly presented in a normalized scale using the code values of manipulated variables (factors) ((Myers et al., 2016)). The code values are convenient for developing general-purpose and specific experimental plans and response surface models.

The experimental design area of the factorial experiment in code values is defined by manipulation ranges for each factor:$1 \leq x_j \leq 1,\ j = 1,\ldots.,n.$where x_j is the code value of j-th manipulated variable (factor); n is the number of manipulated variables in the factorial experiment.

The code variable values $+1$ and -1 define the limitary (max and min) values of the experimental design area.

The real (absolute) values of manipulated variables in the experimental design table are determined using the relationship:

$$x_j^{abs} = x_j \cdot \left(x_{max\ \ j}^{abs} - x_{min\ \ j}^{abs} \right) \Big/ 2 + \left(x_{max\ \ j}^{abs} + x_{min\ \ j}^{abs} \right) \Big/ 2 \quad (11)$$

where x_j^{abs} is the absolute value of the *j*-th factor, x_{jmax}^{abs} and x_{jmin}^{abs} are the max and the min absolute values of the *j*-th factor manipulation range in the experimental design plan.

The code values in Table 6 are taken from a typical experimental design plan developed for 2nd order polynomial model (Hartmann et al., 1974)

Due to significant variation in the experimental results, a logarithmic transformation was applied to reduce dispersion and improve model prediction accuracy. The transformed model is expressed as:

$$\ln(Y) = a_0 + a_1 x_1 + a_2 x_2 + a_{11} x_1^2 + a_{22} x_2^2 + a_{12} x_1 x_2 \quad (12)$$

where Y is the predicted parameter of the adsorption process (adsorption rate or duration); x_1 is the phosphorus ion concentration, g P^{5+}/L; x_2 is the adsorption temperature, °C; a_{ij} are the model parameters identified using the least-squares method (Myers et al., 2016).

The identified parameter values for predicting adsorption rate and duration are given in Table 7.

As shown in Fig. 8a and c, the developed model provided a satisfactory approximation of the experimental data.

According to the response surface-based predictions within the investigated experimental design area (Fig. 8b), the maximum adsorption rate (0.0284 g/l/min) is obtained at an initial phosphorus ion concentration of 0.2 g P^{5+}/L and an adsorption temperature of 33 °C. The minimum adsorption rate (0.000586 g/l/min) is predicted at an initial phosphorus ion concentration of 4.04 g P^{5+}/L and a temperature of 45 °C. As follows from the adsorption rate response surface, the maximum rate for any initial phosphorus ion concentrations is achieved at a temperature within the range 33–35 °C. Moreover, the adsorption rate increases as the initial phosphorus ion concentration decreases.

According to the response surface shown in Fig. 8d, the minimum adsorption duration (3.55 min) is reached at an initial phosphorus ion concentration of 0.2 g P^{5+}/L and an adsorption temperature of 33 °C. The maximum duration (4310 min) is predicted at an initial concentration of 4.52 g P^{5+}/L and a temperature of 45 °C. A temperature range of 33–35 °C minimizes the adsorption duration across all initial phosphorus concentrations. The duration decreases as the initial phosphorus ion concentration decreases.

4. Conclusions

This study demonstrated that calcium–silicate–hydrate (CSH) adsorbents synthesized from CaO and natural opoka effectively remove phosphorus across a wide concentration range (0.2–5.0 g P^{5+}/L). The adsorption capacity increased with increasing initial phosphorus concentration, reaching approximately 270 mg P^{5+}/g, while removal efficiency decreased at higher concentrations (~50% at 5 g P^{5+}/L). At low phosphorus concentrations (0.2 g P^{5+}/L), the adsorbent achieved >98% removal efficiency, confirming its suitability for treating dilute wastewater. The adsorption process was primarily controlled by chemical interactions between calcium silicate hydrate phases (α-C$_2$SH and semi-crystalline CSH) and phosphate ions, resulting mainly in hydroxyapatite formation. Under conditions of high phosphorus concentration and lower temperature, brushite formation was additionally observed, indicating that the reaction pathway depends on both concentration and temperature. Kinetic analysis showed that the adsorption process followed a pseudo-second-order model over the investigated temperature range (25–45 °C), confirming chemisorption as the dominant mechanism. Isotherm modelling indicated that Langmuir, Freundlich, and Temkin models adequately described the adsorption behavior depending on temperature, reflecting the heterogeneous nature of the synthesized material, where tobermorite contributed mainly to physical adsorption and α-C$_2$SH acted as the main chemisorption phase. Response-surface modelling identified optimal adsorption conditions at 33–35 °C and lower initial phosphorus concentrations, where the process proceeded most rapidly. Overall, hydrothermally synthesized CSH from natural minerals represents an efficient and cost-effective adsorbent for phosphorus removal, providing insight into temperature- and concentration-dependent adsorption mechanisms and offering a basis for optimizing phosphorus removal in wastewater treatment.

Funding

This work was funded by the Research Council of Lithuania (LMTLT), Grant No S-MIP-25–4.

CRediT authorship contribution statement

Evelina Svedaite: Writing – original draft, Investigation, Data curation. **Kestutis Baltakys:** Supervision, Project administration, Methodology. **Donatas Levisauskas:** Visualization, Validation, Software. **Vytautas Galvanauskas:** Visualization, Validation, Methodology. **Tadas Dambrauskas:** Writing – review & editing, Formal analysis, Conceptualization.

Declaration of competing interest

The authors declare that they have no known competing financial interests or personal relationships that could have appeared to influence the work reported in this paper.

Supplementary materials

Supplementary material associated with this article can be found, in the online version, at doi:10.1016/j.hazadv.2026.101159.

Data availability

Data will be made available on request.

References

Aigbe, U.O., Ukhurebor, K.E., Onyancha, R.B., Osibote, O.A., Darmokoesoemo, H., Kusuma, H.S., 2021. Fly ash-based adsorbent for adsorption of heavy metals and dyes from aqueous solution: a review. J. Mater. Res. Technol. 14, 2751–2774. https://doi.org/10.1016/j.jmrt.2021.07.140.

Akinnawo, S.O., 2023. Eutrophication: causes, consequences, physical, chemical and biological techniques for mitigation strategies. Environ. Challenges 12, 100733. https://doi.org/10.1016/J.ENVC.2023.100733.

Amarh, F., Voegborlo, R.B., Essuman, E.K., Agorku, E.S., Tettey, C.O., Kortei, N.K., 2021. Effects of soil depth and characteristics on phosphorus adsorption isotherms of different land utilization types: phosphorus adsorption isotherms of soil. Soil Tillage Res. 213, 105139. https://doi.org/10.1016/J.STILL.2021.105139.

Augustyniak-Tunowska, R., Karczmarczyk, R., Łopata, M., Grochowska, J., Tunowski, J., Tandyrak, R., 2023. Characteristics of P adsorption by profundal bottom deposits of Kortowskie Lake (Poland), restored by the hypolimnetic withdrawal method. Appl. Sci. 13 (3), 1861. https://doi.org/10.3390/app13031861.

Barrero, J., Senaldi, C., La Spina, R. and Riego Sintes, J., Interlaboratory comparison on the determination of the Volume Specific Surface Area (VSSA) of Manufactured Nanomaterials, EUR 30702 EN, Publications Office of the European Union, Luxembourg, 2021, ISBN 978-92-76-37685-9, doi:10.2760/41115, JRC124644.

Baruah, S., Neog, D., 2025. Adsorption analysis of organic and chemical sorbents for oil spill management on land. Results. Eng. 26, 105167. https://doi.org/10.1016/J.RINENG.2025.105167.

Bus, A., 2017. Assessment of sorption properties and kinetic reaction of phosphorus reactive material to limit diffuse pollution. Ann. Warsaw Univ. Life Sci. – SGGW. Land Reclamation 49 (3), 143–152. https://doi.org/10.1515/sggw-2017-0012.

Corrado, A., Polini, W., 2019. Measurement of high flexibility components in composite material by touch probe and force sensing resistors. J. Manuf. Process. 45, 520–531. https://doi.org/10.1016/J.JMAPRO.2019.07.038.

Cui, K., Han, X., Zhou, P., Hao, M., Wang, X., Bian, L., Nie, J., Yang, G., Liang, J., Liu, X., Wang, F., 2024. A novel highly dispersed calcium silicate hydrate nanosheets for efficient high-concentration Cu2+ adsorption. J. Hazard. Mater. 475, 134774. https://doi.org/10.1016/J.JHAZMAT.2024.134774.

Dambrauskas, T., Baltakys, K., Eisinas, A., Kitrys, S., 2019. The specific surface area and porosity of synthetic and calcined α-C2SH, kilchoanite and hydroxyledgrewite. Powder. Technol. 355, 504–513. https://doi.org/10.1016/J.POWTEC.2019.07.078.

Gao, D., Zhang, W., Dong, H., Yu, Y., Liu, W., Luo, H., Jing, Z., Liang, B., Peng, L., Wu, B., Huang, T., Cheng, H., 2025. Phosphorus removal from water by the layered double hydroxides (LDHs)-based adsorbents: a review for structure, mechanism, and current progress. Environ. Technol. Innov. 37, 104003. https://doi.org/10.1016/J.ETI.2024.104003.

García-Ávila, F., García-Pizarro, E., Malla-Aguilar, G., Sánchez-Cabrera, C., Cadme-Galabay, M., Valdiviezo-Gonzales, L., Cabello-Torres, R., 2025. Influence of nutrients on aquatic vegetation and trophic status of lakes: analysis of eutrophication and mitigation. Results Eng. 27, 106381. https://doi.org/10.1016/J.RINENG.2025.106381.

Gizaw, A., Zewge, F., Chebude, Y., Tesfaye, M., Mekonnen, A., 2022. A fixed-bed column study of solid waste-based calcium silicate hydrate for the phosphate removal. J. Water Supply 71 (7), 849–861. https://doi.org/10.2166/aqua.2022.167.

Goldsberry, P., Jeppesen, P., McLean, J., Sims, R., 2023. An attached microalgae platform for recycling phosphorus through biologically mediated fertilizer formation and biomass cultivation. Clean. Eng. Technol. 17, 100701. https://doi.org/10.1016/J.CLET.2023.100701.

Han, M., Shen, X., Shao, H., Liu, Y., Han, Q., Zhai, Y., 2023. Facile one-pot hydrothermal synthesis of reticulated porous tobermorite for fast phosphorus recovery. Colloids Surfaces A 666, 131349. https://doi.org/10.1016/j.colsurfa.2023.131349.

Hao, M., Li, H., Cui, L., Liu, W., Fang, B., Liang, J., Xie, X., Wang, D., Wang, F., 2021. Higher photocatalytic removal of organic pollutants using pangolin-like composites made of 3–4 atomic layers of MoS2 nanosheets deposited on tourmaline. Environ. Chem. Lett. 19 (5), 3573–3582. https://doi.org/10.1007/s10311-021-01235-6.

Hartmann, K., Lezki, E., Schafer, W., 1974. Statistische Versuchsplanung und –answertung in Der Stoffwirtschaft. VEB Deutscher Verlag fur Grundstoffindustrie.

Hernández-Alcayaga, N., Crutchik, D., 2025. Strategies to enhance the recovery of phosphorus as struvite during the storage of urine. Results. Eng. 25, 103707. https://doi.org/10.1016/J.RINENG.2024.103707.

Huo, J., Min, X., Wang, Y., 2021. Zirconium-modified natural clays for phosphate removal: effect of clay minerals. Environ. Res. 194, 110685. https://doi.org/10.1016/j.envres.2020.110685.

Karageorgiou, K., Paschalis, M., Anastassakis, G.N., 2007. Removal of phosphate species from solution by adsorption onto calcite used as natural adsorbent. J. Hazard. Mater. 139 (3), 447–452. https://doi.org/10.1016/J.JHAZMAT.2006.02.038.

Kari-Ferro, A., Solano-Reynoso, A.M., Alvarez-Arias, C., Echegaray-Peña, N.G., Choque-Quispe, D., 2024. Activated polymeric materials for phosphorus removal in aqueous medium: study of kinetics and adsorption isotherm. Results. Eng. 24, 103201. https://doi.org/10.1016/J.RINENG.2024.103201.

Kim, E.H., Yim, S.B., Jung, H.C., Lee, E.J., 2006. Hydroxyapatite crystallization from a highly concentrated phosphate solution using powdered converter slag as a seed material. J. Hazard. Mater. 136 (3), 690–697. https://doi.org/10.1016/J.JHAZMAT.2005.12.051.

Kong, C., Liu, L., Yang, X., Lu, F., 2025. Study on the adsorption mechanism of ricinoleate and oleate on kaolinite and quartz surfaces. Miner. Eng. 232, 109544. https://doi.org/10.1016/J.MINENG.2025.109544.

Lade, V.G. (.2021). Introduction of water remediation processes. *Handbook of Nanomaterials for Wastewater treatment: fundamentals and scale up issues*, 741–777. https://doi.org/10.1016/B978-0-12-821496-1.00033-7.

Maimulyanti, A., Nurhidayati, I., Widarsih, R.W., 2022. Adsorption isotherm models and kinetics for phosphate ADSORPTION in sediment. RASAYAN J. Chem. 15 (04), 2626–2631. https://doi.org/10.31788/RJC.2022.1546819.

Manna, A., Naskar, N., Sen, K., Banerjee, K., 2022. A review on adsorption mediated phosphate removal and recovery by biomatrices. J. Indian Chem. Soc. 99 (10), 100682. https://doi.org/10.1016/J.JICS.2022.100682.

Mechnou, I., Benabdallah, A., Chham, A.I., Rachdi, Y., Hlaibi, M., El kartouti, A., Saleh, N., 2025. Activated carbons for effective pharmaceutical adsorption: impact of feedstock origin, activation agents, adsorption conditions, and cost analysis. Results Eng. 27, 105966. https://doi.org/10.1016/J.RINENG.2025.105966.

Moharami, S., Jalali, M., 2013. Removal of phosphorus from aqueous solution by Iranian natural adsorbents. Chem. Eng. J. 223, 328–339. https://doi.org/10.1016/j.cej.2013.02.114.

Moussavi, G., Khosravi, R., 2010. Removal of cyanide from wastewater by adsorption onto pistachio hull wastes: parametric experiments, kinetics and equilibrium analysis. J. Hazard. Mater. 183 (1–3), 724–730. https://doi.org/10.1016/j.jhazmat.2010.07.086.

Myers, R.H., Montgomery, D.C., Anderson-Cook, C.M., 2016. Response Surface Methodology: Process and Product Optimization Using Designed Experiments. Wiley.

Nakić, D., Licht, K., Posavčić, H., Halkijević, I., 2025. Biochar from experimental sewage sludge gasification as an adsorbent for phosphate removal. Results. Eng. 27, 106077. https://doi.org/10.1016/J.RINENG.2025.106077.

Nguyen, M.D., Donaldson, D., Adhikari, S., Amini, N., Mallya, D.S., Thomas, M., Moon, E. M., Milne, N.A., 2023. Phosphorus adsorption and organic release from dried and thermally treated water treatment sludge. Environ. Res. 234, 116524. https://doi.org/10.1016/j.envres.2023.116524.

Ou, E., Zhou, J., Mao, S., Wang, J., Xia, F., Min, L., 2007. Highly efficient removal of phosphate by lanthanum-doped mesoporous SiO2. Colloids Surfaces A 308 (1–3), 47–53. https://doi.org/10.1016/j.colsurfa.2007.05.027.

Ozcan, D.O., Hendekci, M.C., Ovez, B., 2024. Enhancing the adsorption capacity of organic and inorganic pollutants onto impregnated olive stone derived activated carbon. Heliyon. 10 (12), e32792. https://doi.org/10.1016/J.HELIYON.2024.E32792.

Phawachalotorn, C., Wongniramaikul, W., Taweekarn, T., Kleangklao, B., Pisitaro, W., Limsakul, W., Sriprom, W., Towanlong, W., Choodum, A., 2023. Continuous phosphate removal and recovery using a calcium silicate hydrate composite monolithic cryogel column. Polymers (Basel) 15 (3), 539. https://doi.org/10.3390/polym15030539.

Piao, Y., Jiang, Q., Li, H., Matsumoto, H., Liang, J., Liu, W., Pham-Huu, C., Liu, Y., Wang, F., Liu, W., Wang, F., 2020. Identify Zr promotion effects in atomic scale for Co-based catalysts in Fischer-Tropsch synthesis. ACS. Catal. 10 (14), 7894–7906. https://doi.org/10.1021/acscatal.0c01874.

Pimentel Frisancho, J.P., Miranda Ramos, L.M., Delgado Sarmiento, P.K., Alvarez Tohalino, V.L., Tejada Manrique, E.E., Saavedra Campos, J.C., Quispe Ortiz, J.A., Sanchez Sarmiento, D.C., Jiménez Pacheco, H.G, 2025. Efficient adsorption of Pb2+ from aqueous solutions using papain immobilized on alginate beads. Results. Eng. 27, 105886. https://doi.org/10.1016/J.RINENG.2025.105886.

Rezania, S., Kamyab, H., Rupani, P.F., Park, J., Nawrot, N., Wojciechowska, E., Yadav, K. K., Lotfi Ghahroud, M., Mohammadi, A.A., Thirugnana, S.T., Chelliapan, S., Cabral-Pinto, M.M.S., 2021. Recent advances on the removal of phosphorus in aquatic plant-based systems. Environ. Technol. Innov. 24, 101933. https://doi.org/10.1016/J.ETI.2021.101933.

Riza, M., Ehsan, M.N., Pervez, M.N., Khyum, M.M.O., Cai, Y., Naddeo, V., 2023. Control of eutrophication in aquatic ecosystems by sustainable dredging: effectiveness, environmental impacts, and implications. Case Stud. Chem. Environ. Eng. 7, 100297. https://doi.org/10.1016/J.CSCEE.2023.100297.

Salkunić, A., Vuković, J., Smiljanić, S., 2022. Review of technologies for the recovery of phosphorus from waste streams. Chem. Biochem. Eng. Q. 2. https://doi.org/10.15255/CABEQ.2022.2066.

Samantray, J., Anand, A., Dash, B., Ghosh, M.K., Behera, A.K., 2022. Silicate minerals - Potential source of potash - A review. Miner. Eng. 179, 107463. https://doi.org/10.1016/J.MINENG.2022.107463.

Siauciunas, R., Smalakys, G., Dambrauskas, T., 2021. Porosity of calcium silicate hydrates synthesized from natural rocks. Materials. (Basel) 14 (19), 5592. https://doi.org/10.3390/ma14195592.

Singh, S., Garg, R., Jana, A., Bathula, C., Naik, S., Mittal, M., 2023. Current developments in nanostructurally engineered metal oxide for removal of contaminants in water. Ceram. Int. 49 (5), 7308–7321. https://doi.org/10.1016/J.CERAMINT.2022.10.183.

Soo, X.Y.D., Lee, J.J.C., Wu, W.Y., Tao, L., Wang, C., Zhu, Q., Bu, J., 2024. Advancements in CO2 capture by absorption and adsorption: a comprehensive review. J. CO2 Util. 81, 102727. https://doi.org/10.1016/J.JCOU.2024.102727.

Sun, Z., Tian, C., Yang, T., Fu, J., Xu, H., Wang, Y., Lin, Z., 2022. A MOF-based trap with strong affinity toward low-concentration heavy metal ions. Sep. Purif. Technol. 301, 121946. https://doi.org/10.1016/j.seppur.2022.121946.

Tan, K.L., Hameed, B.H., 2017. Insight into the adsorption kinetics models for the removal of contaminants from aqueous solutions. J. Taiwan. Inst. Chem. Eng. 74, 25–48. https://doi.org/10.1016/j.jtice.2017.01.024.

Tang, S., Wang, Y., Geng, Z., Xu, X., Yu, W., A, H., Chen, J., 2021. Structure, fractality, mechanics and durability of calcium silicate hydrates. Fractal Fractional 5 (2), 47. https://doi.org/10.3390/fractalfract5020047.

Taweekarn, T., Wongniramaikul, W., Choodum, A., 2022. Removal and recovery of phosphate using a novel calcium silicate hydrate composite starch cryogel. J. Environ. Manage 301, 113923. https://doi.org/10.1016/J.JENVMAN.2021.113923.

Taweekarn, T., Wongniramaikul, W., Roop-o, P., Towanlong, W., Choodum, A., 2023. Recovering phosphate from complex wastewater using macroporous cryogel composited calcium silicate hydrate nanoparticles. Molecules 29 (1), 228. https://doi.org/10.3390/molecules29010228.

Thommes, M., Kaneko, K., Neimark, A.V., Olivier, J.P., Rodriguez-Reinoso, F., Rouquerol, J., Sing, K.S.W., 2015. Physisorption of gases, with special reference to the evaluation of surface area and pore size distribution (IUPAC Technical Report). Pure Appl. Chem. 87 (9–10), 1051–1069. https://doi.org/10.1515/pac-2014-1117.

Trotta, S., Adani, F., Fedele, M., Salvatori, M., 2023. Nitrogen and phosphorus recovery from cow digestate by struvite precipitation: process optimization to maximize phosphorus recovery. Results. Eng. 20, 101478. https://doi.org/10.1016/J.RINENG.2023.101478.

Wang, F., Xie, Z., Liang, J., Fang, B., Piao, Y., Hao, M., Wang, Z., 2019. Tourmaline-modified FeMnTiOx catalysts for improved low-temperature NH3-SCR performance. Environ. Sci. Technol. 53 (12), 6989–6996. https://doi.org/10.1021/acs.est.9b02620.

Wen, X., Huang, F., Gao, W., Luo, Z., Zhang, B., Liu, R., Cao, C., Shi, W., Zhang, G., 2024. Three-dimensional observation of porous materials prepared from iron tailings and their pore wall site adsorption function. Ceram. Int. 50 (5), 7663–7672. https://doi.org/10.1016/J.CERAMINT.2023.12.090.

Wu, X., Liu, S., Song, S., Liu, Y., Huang, C., Wang, L., He, J., Shen, F., Zhang, Y., 2024. Calcium silicate hydrate complex konjac glucomannan-based hydrogel selectively adsorbed phosphate in low alkalinity solution. J. Environ. Manage 370, 122560. https://doi.org/10.1016/j.jenvman.2024.122560.

Wujcicki, Ł., Kluczka, J., 2023. Recovery of phosphate(V) ions from water and wastewater using Chitosan-based sorbents modified—a literature review. Int. J. Mol. Sci. 24 (15), 12060. https://doi.org/10.3390/ijms241512060.

Zhang, Z., Wang, X., Zhao, J., 2019. Phosphate recovery from wastewater using calcium silicate hydrate (C-S-H): sonochemical synthesis and properties. Environ. Sci. 5 (1), 131–139. https://doi.org/10.1039/C8EW00643A.

Zheng, Y., Wan, Y., Zhang, Y., Huang, J., Yang, Y., Tsang, D.C.W., Wang, H., Chen, H., Gao, B., 2023. Recovery of phosphorus from wastewater: a review based on current phosphorous removal technologies. Crit. Rev. Environ. Sci. Technol. 53 (11), 1148–1172. https://doi.org/10.1080/10643389.2022.2128194.

Zheng, E., Feng, G., Jiang, F., Shao, C., Fu, H., Hu, Z., Wu, Q., Yang, Q., Liu, J., 2024. Effect of process parameters on the synthesis and lead ions removal performance of novel porous hydroxyapatite sheets prepared via non-aqueous precipitation method. Ceram. Int. 50 (7), 10897–10905. https://doi.org/10.1016/J.CERAMINT.2023.12.406.